Journal of Power Sources 343 (2017) 127–134

Contents lists available at ScienceDirect

Journal of Power Sources

journal homepage: www.elsevier.com/locate/jpowsour

The surface evolution of $La_{0.4}Sr_{0.6}TiO_{3+\delta}$ anode in solid oxide fuel cells: Understanding the sulfur-promotion effect

Ning Yan [a, b, *], Sandrine Zanna [c], Lorena H. Klein [c], Milad Roushanafshar [a], Babak S. Amirkhiz [d], Yimin Zeng [d], Gadi Rothenberg [b], Philippe Marcus [c, **], Jing-Li Luo [a, ***]

[a] Department of Chemical and Materials Engineering, University of Alberta, T6G 1H9, Edmonton, Alberta, Canada
[b] Van't Hoff Institute for Molecular Sciences (HIMS), University of Amsterdam, 1098XH, Amsterdam, The Netherlands
[c] PSL Research University, Chimie ParisTech-CNRS, Institut de Recherche de Chimie Paris, Research Group Physical Chemistry of Surfaces, 11 rue Pierre et Marie Curie, F-75005, Paris, France
[d] CanmetMATERIALS, Natural Resources Canada, L8P 0A5, Hamilton, Ontario, Canada

HIGHLIGHTS

- $La_{0.4}Sr_{0.6}TiO_{3+\delta}$ anode underwent surface amorphization in solid oxide fuel cells.
- Various adsorbed sulfur species formed when exposed to H_2S-containing fuels.
- These sulfur species promoted the fuel conversion in SOFC.

GRAPHICAL ABSTRACT

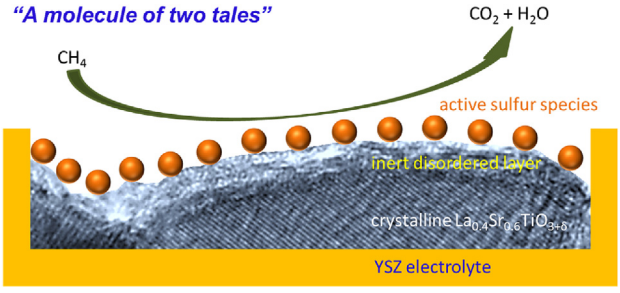

ARTICLE INFO

Article history:
Received 6 November 2016
Received in revised form
7 December 2016
Accepted 9 January 2017

Keywords:
Titanate
Sulfur poisoning
Sulfur promoter
Surface chemistry
Quenching

ABSTRACT

The ideal solid oxide fuel cells (SOFCs) can be powered by readily available hydrocarbon fuels containing impurities. While this is commonly recognized as a key advantage of SOFC, it also, together with the elevated operating temperature, becomes the main barrier impeding the *in-situ* or *operando* investigations of the anode surface chemistry. Here, using a well-designed quenching experiment, we managed to characterize the near-surface structure of $La_{0.4}Sr_{0.6}TiO_{3+\delta}$ (LST) anode in SOFCs fuelled by H_2S-containing methane. This new method enabled us to clearly observe the surface amorphization and sulfidation of LST under simulated SOFC operating conditions. The ~1 nm-thick two dimensional sulfur-adsorbed layer was on top of the disordered LST, containing −S, −SH and elemental sulfur species. In SOFC test, such "poisoned" anode showed increased performances: a ten-fold enhanced power density enhancement (up to 30 mW cm^{-2}) and an improved open circuit voltage (from 0.69 V to 1.17 V). Moreover, its anodic polarization resistance in methane decreased to 21.53 Ω cm^2, a difference of 95% compared with the sulfur-free anode. Control experiments confirmed that once the adsorbed sulfur species were removed electrochemically, methane conversion slowed down simultaneously till full stop.

* Corresponding author. University of Amsterdam, Van't Hoff Institute for Molecular Sciences, Science Park 904, 1098XH, Amsterdam, The Netherlands.
** Corresponding author.
*** Corresponding author. Department of Chemical and Materials Engineering, University of Alberta, T6G 1H9, Edmonton, Alberta, Canada.
E-mail addresses: n.yan@uva.nl (N. Yan), philippe.marcus@chimie-paristech.fr (P. Marcus), jingli.luo@ualberta.ca (J.-L. Luo).

http://dx.doi.org/10.1016/j.jpowsour.2017.01.048
0378-7753/

1. Introduction

Fuel diversity is, supposedly, one of the most advantageous features of solid oxide fuel cells (SOFCs) [1–3]. The high operating temperature grants direct conversion of economically viable fossil fuels into power cleanly and efficiently. But in practice, theses impurity-containing feedstocks, such as natural gas and biogas with H_2S contaminant, deactivate many anode catalysts significantly, causing severe coking and/or sulfur poisoning problems [4–11]. Indeed, optimizing the fuel cell operating parameters is a fairly practical way of minimizing the poisoning effects [12]. Replacing the state-of-the-art Ni cermet with alternatives or engineering the microstructures of the anode seems open more opportunities to alleviate such deactivation. For instance, bimetallic alloys [13], simple oxides [14,15], and complex oxides such as doped perovskite oxides were all among the most promising candidates [7,16–19]. Good SOFC performances were also reported when the anode structure was engineered: a typical measure is to add uniformly-dispersed active nanoparticles on perovskite backbones to boost the electrochemical reaction rate [20–23].

While most of the current approaches are unable to fully suppress the sulfur poisoning effect, the extensive studies also revealed an interesting phenomenon: as a notorious catalyst poison, H_2S, in many cases, can be a catalyst as well (namely, promoter), leading to the catalytic performance increase [24–27]. These seemingly contradictory results reflect the lack of understanding of the interaction between the anode catalyst and H_2S under SOFC operating environment. However, on one hand, the conventional *ex-situ* approach analyzing regular "cooled" sample was inappropriate, especially when studying the surface chemistry: the reactions of the surface absorbants and the catalyst can happen readily during the slow cooling process [12]. On the other hand, hydrogen sulfide is highly toxic and corrosive, it is inherently an uneasy task to characterize the anode materials exposed to H_2S at elevated temperature using either *in-situ* or *operando* techniques. Since the pioneering work by Walker's and Liu's groups using *in-situ* Raman approach [28,29], *operando* optical and XANES (fluorescence-detection mode) methods were also developed recently to investigate the interactions between adsorbed sulfur species and the catalyst [30,31]. Nonetheless, these methods were surface non-sensitive and used only for the bulk properties examination of the catalyst.

In this work, using a well-tailored quenching test, we managed to characterize the surface structure evolution of $La_{0.4}Sr_{0.6}TiO_{3+\delta}$ (LST) anode in SOFCs fuelled by H_2S-containing methane. This facile method helps us explore the sulfur promoting effects of methane conversion in intermediate-temperature SOFCs.

2. Experimental

2.1. Materials and instrumentation

$La_{0.4}Sr_{0.6}TiO_{3+\delta}$ (LST) samples, for both powder and disc, were prepared via a classic solid-state reaction. The disc sample was densified at 1400 °C. In the annealing-quenching test, the samples were placed in a sealed quartz tube that was heated up to 850 °C under vacuum ($<10^{-4}$ mbar). After annealing in H_2, 0.5% H_2S–H_2 and 0.5% H_2S–CH_4 for 30 min, the tube, along with the samples, was immediately quenched to room temperature using ice water within 10 s. Therefore, the possible parasitic reactions during the cooling process were eliminated; both the surface composition and morphology were maintained to room temperature for further measurements. Note that the composition of the simulated fuel atmosphere may vary compared with that in a biased SOFC as a result of electrochemical oxidation.

X-ray diffraction (XRD) patterns were obtained on a Miniflex II diffractometer using Ni-filtered Cu Kα radiation. The X-ray tube was operated at 30 kV and 15 mA. Temperature programmed reduction (TPR) measurement in hydrogen was done on a Thermo TPDRO 1100 instrument using a thermal conductivity detector (TCD). 50 mg of LST was placed in the reactor and TPR was measured under 5% H_2 in a N_2 flow (30 mL min^{-1}), heating at 5 °C min^{-1} from 30 °C to 1000 °C. Transmission electron microscopy (TEM) analyses were performed using a JEOL-JEM 2100 microscope. Scanning transmission electron microscopy (STEM) analyses were carried out using a FEI's Tecnai Osiris microscope equipped with high angle annular dark field (HAADF) STEM detector. ChemiSTEM X-ray detection technology was employed to characterize the sample chemistry. The microstructure of SOFC was investigated using a field emission scanning electron microscope (FE-SEM, JOEL 6301F).

Time-of-flight secondary ion mass spectrometer (ToF-SIMS) and X-ray photoelectron spectroscopy (XPS) measurements were performed using an ION-TOF ToF-SIMS spectrometer and a VG ESCALAB 250 XPS spectrometer. In ToF-SIMS measurement, a pulsed 25 keV Bi^+ primary ion source delivering a 1.3 pA current was used over a 100 × 100 μm^2 area. Depth profiling was performed by sputtering with a 0.5 keV Cs^+ ion gun giving a 25 mA target current over a 300 × 300 μm^2 raster area. Data acquisition and post processing analyses were performed using the ION-Spec software. For the XPS measurements, a monochromated Al Kα ($h\nu = 1486.6$ eV) source was used as the power, the base pressure in the analytical chamber was maintained at 10^{-9} mbar. The obtained spectra were analyzed using the Thermo Avantage software calibrated to the C 1s binding energy of 285.0 eV. For curve fitting and deconvolution, a Shirley-type background subtraction and a Gaussian-Lorentzian peak shape were applied. HSC Chemistry 5.0 was used to perform thermodynamic calculations.

2.2. The SOFC test rig

The detailed fabrication procedures of membrane electrode assembly (MEA) have been described in our previous work [23]. Briefly, two porous yttria-stabilized zirconia (YSZ) matrix electrodes were initially applied on the opposite sides of a commercial YSZ disc (300 μm thick, 25 mm in diameter) via screen printing and 1200 °C sintering. Both electrodes were ~35 μm thick. To fabricate the cathode, a barrier layer composed of 10 wt% $Gd_{0.2}Ce_{0.8}O_2$ (GDC) was initially infiltrated into one porous YSZ electrode matrix before subsequent impregnation of 16 wt% $La_{0.6}Sr_{0.4}Co_{0.2}Fe_{0.8}O_3$ (LSCF). 16 wt% of LST was infiltrated into the other porous YSZ matrix as the anode. The final 900 °C calcination was 2 h to acquire the desired crystal phases of the electro-catalysts.

The MEA was fixed and sealed between a pair of coaxial alumina tubes accommodated in the furnace. Hydrogenation and H_2S treatment were performed at 850 °C in certified 5000 ppm $H_2S + H_2$ (Praxair), respectively. The obtained black LST and sulfur-adsorbed black LST were denoted as B-LST and S/B-LST, respectively. The exhaust of the anode tube was guided to a mass spectrometer (Pfeiffer Thermostar GSD 301) for analysis. Electrochemical analyses were performed using a Solartron SI 1287 electrochemical interface equipped with a SI 1260 impedance/gain-phase analyzer. The AC impedance spectra were obtained at open circuit with a potential perturbation of ±10 mV and a frequency range from 10^5 Hz to 0.01 Hz.

3. Results and discussion

3.1. Surface-disordered LST under SOFC operating conditions

Fig. 1a schematically shows the steps of the annealing-

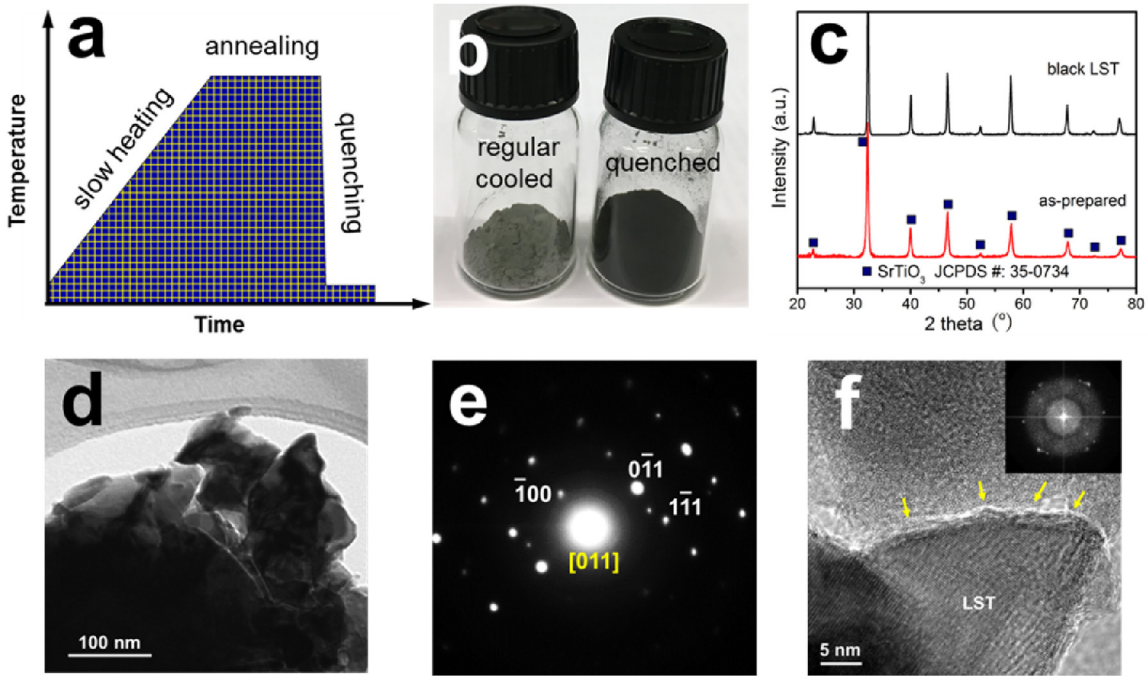

Fig. 1. (a) a schematic temperature-time profile of the annealing-quenching test; (b) photos of LST powder after 0.5 h annealing, followed by either regular cooling or quenching; (c) XRD patterns of as-prepared and black LST. TEM micrographs of B-LST: (d) BF image; (e) SAED pattern of [011] zone axis; (f) HRTEM image with surface disorder indicated by arrows, inset is the diffractogram.

quenching test. A schematic drawing of the test setup was shown in Scheme S1 in the Supporting Information (SI). Remarkably, after 0.5 h treatment in either H_2 or 0.5%H_2S–H_2, the quenched sample became completely dark. In contrast, the regular-cooled LST (cooling rate was *ca.* 3 °C min^{-1}) was greyish (see Fig. 1b). XRD patterns in Fig. 1c indicate no bulk phase transformations occurred after such hydrogenation. There was no chemical reaction between hydrogen and LST either, as indicated by the stable hydrogen signal in the H_2-TPR analysis up to 1000 °C (see Fig. S1 in the SI). Therefore, we postulated that the surface reaction caused such discoloration.

Accordingly, we examined the electronic structures of B-LST using XPS (see Fig. S2 in the SI). The binding energies of Ti 2p3/2 and Ti 2p1/2 for LST were observed at 458.1 eV and 464.5 eV, respectively, well correlated with Ti^{4+} of $SrTiO_3$. Upon hydrogenation-quenching in H_2 or 0.5%H_2S–H_2, however, new oxidation state (Ti^{3+}) or peak shift was not observed. This confuted the formation of defects such as oxygen vacancies or Ti^{3+} through Eq. (1) [32–34].

$$H_2 + O_o^x + 2Ti_{Ti^{4+}}^{4+x} \rightarrow H_2O + V_o^{\cdot\cdot} + 2Ti_{Ti^{4+}}^{3+'} \quad (1)$$

Hence, excess oxygen in B-LST was sustained which was in good agreement with the literature [35]. This conclusion was also supported by the O 1s spectra in Fig. S2b. The spectrum of LST could be deconvoluted into two peaks at 530.1 eV and 532.1 eV, attributed to Ti–O and –OH species, respectively. However, after hydrogenation, no –OH species could be found and the new peak (531.6 eV) could be assigned to oxygen excess [36].

The surface reaction associated with the discoloration was finally identified in TEM analysis. The bright field (BF) image in Fig. 1d demonstrates the microstructure of B-LST particles deposited on YSZ support. Their crystallographic phase was determined by the selected area electron diffraction (SAED) pattern in Fig. 1e ([011] zone axis). The high resolution TEM (HR-TEM) micrograph in Fig. 1f shows the well-resolved lattice features of B-LST. A disordered surface layer, ~3 nm thick, could be seen near the edge of the grain as indicated by the arrows. The diffractogram inset also shows a diffuse halo, implying the presence of amorphous phase. This observation was in accordance with the defects image of doped $SrTiO_3$ materials in the literature [34], and was also found in hydrogenated $SrTiO_3$ and TiO_2 [37]. Conversely, we did not observe such apparent amorphous shell on grey LST (reduced and regular-cooled, see Fig. S3), presumably due to the re-crystallization during the slow cooling process. Thus, we trust that under SOFC anode operating condition (elevated temperature & reducing atmosphere), LST would loss the surface crystallinity, resulting in the discoloration and the formation of a surface disordered layer.

3.2. Interactions of sulfur adsorbate and disordered layer

We then examined how black LST interacted with sulfur after sulfidation in 0.5%H_2S–H_2. Bulk LST has been proven stable against H_2S attack widely [7], but their interaction on the surface was not fully clear. We firstly investigated this surface using TEM and energy-dispersive X-ray spectroscopy (EDS). Noticeably, O, Sr, La and Ti elements were uniformly distributed across the entire region without segregations (see Fig. S4). A tiny peak at 2.3 eV that matched up with sulfur was ascribed to the adsorbed sulfur species. Indeed, such sulfur-substrate interaction can lead to the formation of a 2-D sulfide layer on the surface [12]. For instance, the following reaction might occur in this study:

$$LaTiO_3 + H_2S \rightarrow La_2S_3 + TiO_2 + H_2 + H_2O \quad (2)$$

$$SrTiO_3 + H_2S \rightarrow SrS + TiO_2 + H_2O \quad (3)$$

However, no binding energy shifts of Sr $3d_{5/2}$ (132.7 eV) and La $3d_{5/2}$ (839.2 eV) were observed after either reduction or sulfidation, suggesting that the surface sulfide layer did not form in this

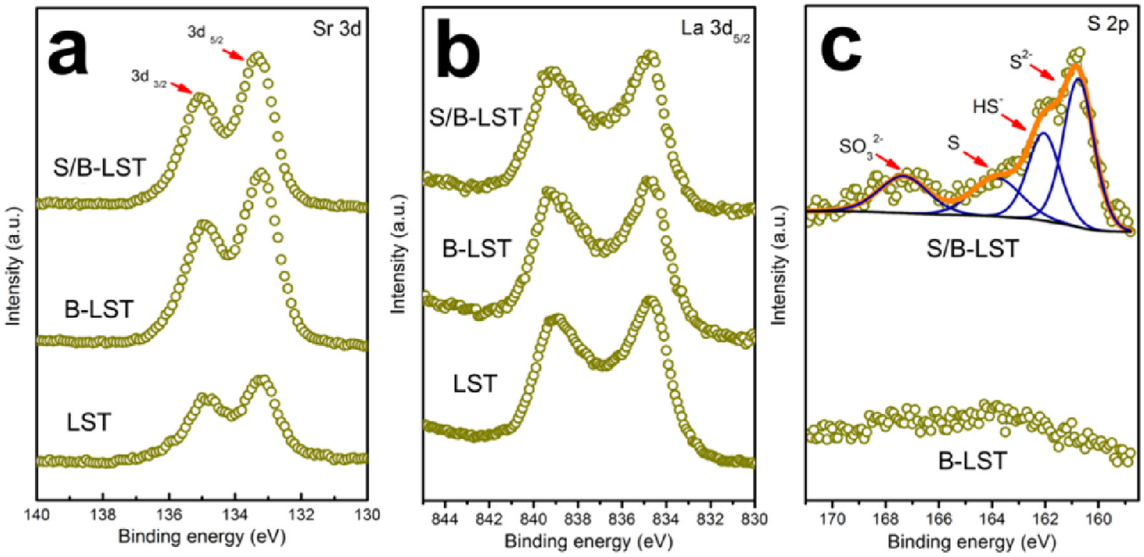

Fig. 2. High resolution XPS spectra of LST, B-LST and S/B-LST for: (a) Sr 3d, (b) La 3d5/2 and (c) S 2p.

experiment (see Fig. 2, *cf.* the XPS spectra in Fig. S2). The additional peak of La was assigned to a shake-up satellite caused by the transfer of a valence-band electron to an empty 4f orbital, which occurred with the transition of a 3d electron to a continuum state [38]. This satellite structure was common in trivalent lanthanum compounds including oxides [39].

Fig. 2c compares S 2p core level XPS spectra of B-LST and S/B-LST. After sulfidation, a broad sulfur peak appeared for S/B-LST. The peak at 160.8 eV could be assigned to the chemisorbed −S (S^{2-}) bounded with metal centers (it is also possible that the surface oxygen anions were substituted by sulfur anions). At 162.1 eV, the peak was correlated with −SH species (HS^{-}). The one at 163.7 eV was related to elemental sulfur atoms that were physically adsorbed on black LST. Another detectable peak located at 167.4 eV was attributable to the formation of sulfite (SO_3^{2-}) that might be produced due to the slight oxidation of reduced sulfur species during the sample transfer from the reactor to the XPS analysis chamber [40].

The thickness of these sulfur species was determined using the equations developed Carlson and ourselves [41–43]:

$$I_s = K \times \delta_s \times \lambda_s^s \times D_s \times T_s \times \left[1 - \exp\left(-\frac{d}{\lambda_s^s}\right)\right] \quad (4)$$

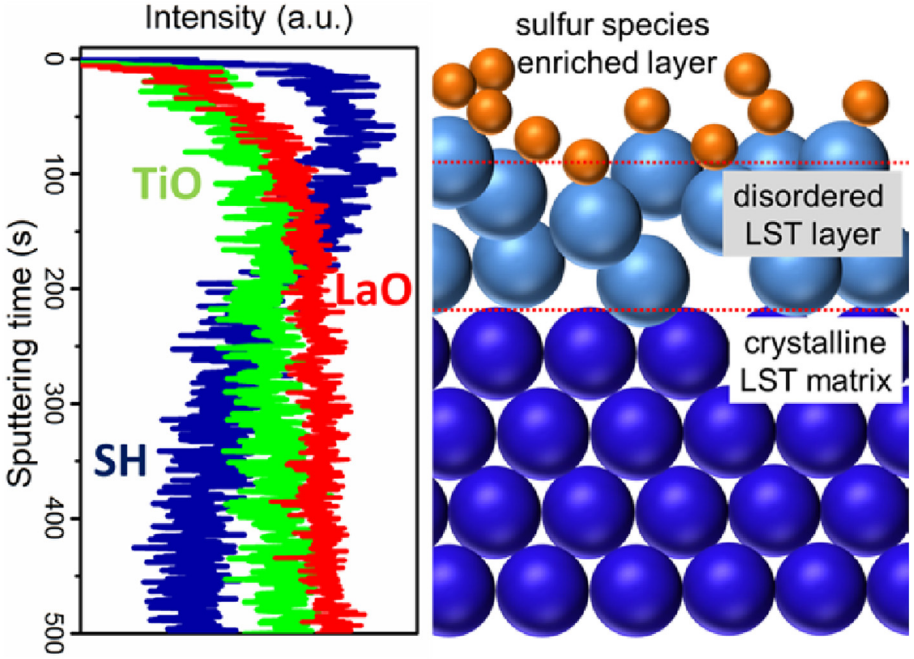

Fig. 3. TOF-SIMS depth profile of negative ions and a schematic of near-surface structure of S/B-LST.

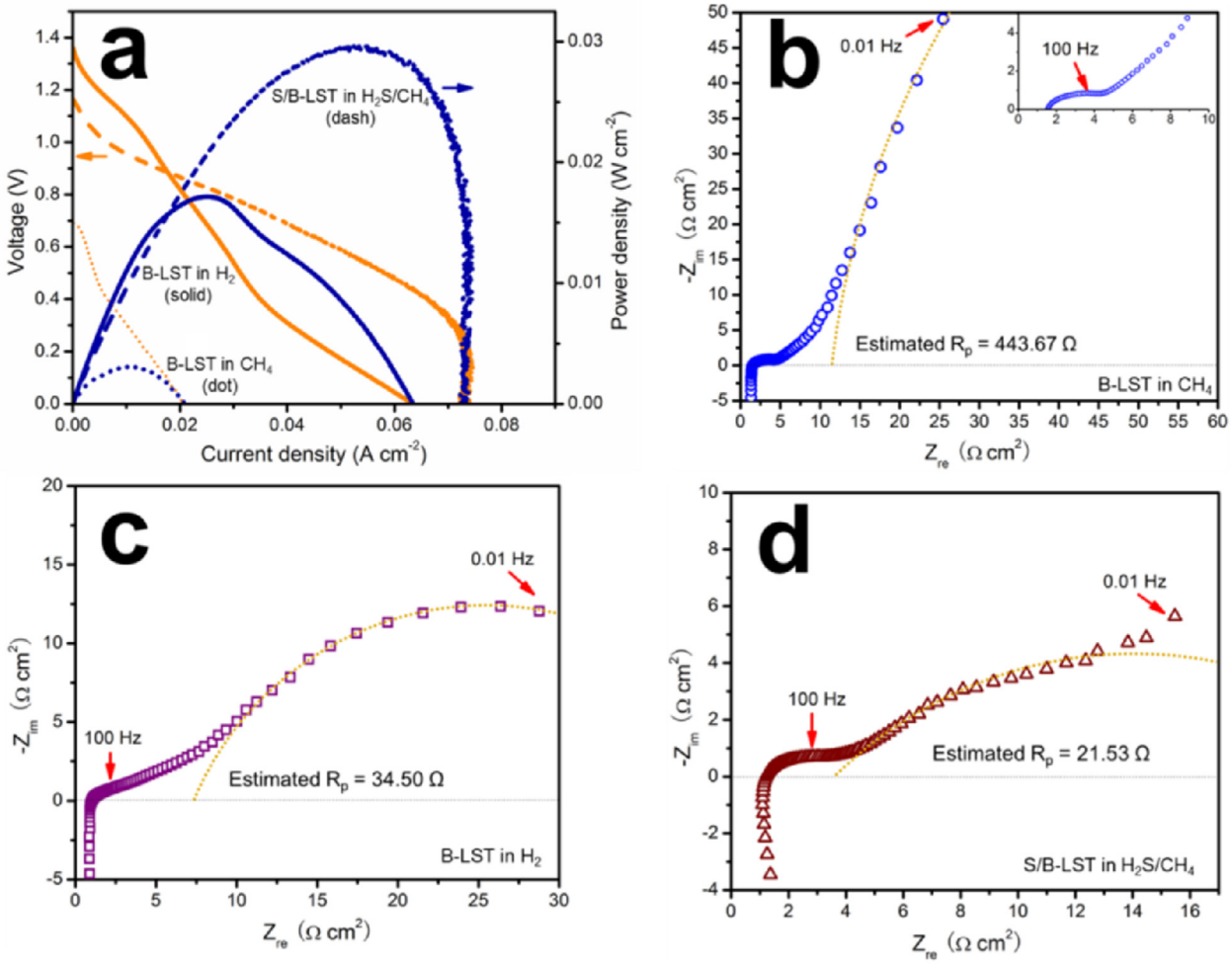

Fig. 4. Comparisons of electrochemical performances of LST based SOFC at 800 °C: (a) I-V plots; impedance spectra for cells in (b) methane, (c) H_2 and (d) 5000 ppm $H_2S + CH_4$. Software ZView was applied to draw the equivalent circuit from which the fitted curves (dotted line) were obtained. Thus, the length between the two intercepts (only the low intercept was drawn in the figure) with $-Z_{im} = 0$ axis represented the charge transfer resistance of the anode (R_p).

$$I_{Ti} = K \times \delta_{Ti} \times \lambda_{Ti}^{LST} \times D_{LST} \times T_{Ti} \times \exp\left(-\frac{d}{\lambda_{Ti}^{s}}\right) \quad (5)$$

where I is the enclosed area under the peak, obtained from Fig. 2c and Fig. S2a, δ is the photoemission cross section of the emitted photoelectrons, λ is the inelastic mean free path (IMFP), D is the atomic concentration, T is the transmission factor determined by the particular machine, K is an apparatus constant and d is the thickness of surface deposits. The calculated thickness d was *ca.* 1.03 nm and did not vary significantly as a function of sulfidation time (see the parameter values in Table S1). We thus concluded that under SOFC operating condition in H_2S-containing methane, the LST surface was eventually a mixture of −S, −SH and elemental S.

Fig. 3 shows the ToF-SIMS depth profile of S/B-LST sample. A signal of SH^- was seen, supporting the XPS result in Fig. 2c. Its intensity reached a maximum initially, implying that the surface layer was rich in sulfur species. As the sputtering proceeded, signals of SH^- started to drop whereas those of LaO^- and TiO^- fragments concurrently began to increase till surpassing that of SH^-. This meant that the probing ion-beam has reached the LST substrate. Accordingly, we drew the schematic of the near-surface structure of sulfur-adsorbed B-LST in Fig. 3 (*c.f.* the TEM and XPS analyses).

3.3. Electrocatalytic promoting effects of adsorbed sulfur species

After determining the surface structure of LST in H_2S-containing fuels, we explored both the structure-activity correlation and the sulfur-promoting effects in SOFC. The operating temperature was selected at 800 °C to minimize the intrinsic activity of LST [44,45]. We found that the open circuit voltage (OCV) in methane was merely 0.69 V, far below the Nernst potential, suggesting that methane molecule was hardly activated (see Fig. 4a). It was then not surprising that the maximum power density (MPD) was 3 mW cm^{-2}. The performance was slightly better in H_2, showing a MPD of 17 mW cm^{-2}. However, when SOFC was fed by 0.5% H_2S—CH_4 (note that H_2S was to create and retain surface sulfur species), the OCV was greatly promoted to 1.17 V from 0.69 V whereas the MPD rose to 30 mW cm^{-2}, even exceeding that in H_2.

In the corresponding impedance measurement, the ohmic resistances of all cells were very close; the semi-circles in the high frequency region (>100 Hz) in all plots were roughly identical, suggesting that the contribution from the GDC-LSCF cathode might predominate (see the overlaid spectra in Fig. S5) [46]. In the low-frequency region till 0.01 Hz, the spectra differed remarkably, shedding some light on the varied anode electro-catalytic behaviors. B-LST showed a huge charge transfer resistance (R_p) in

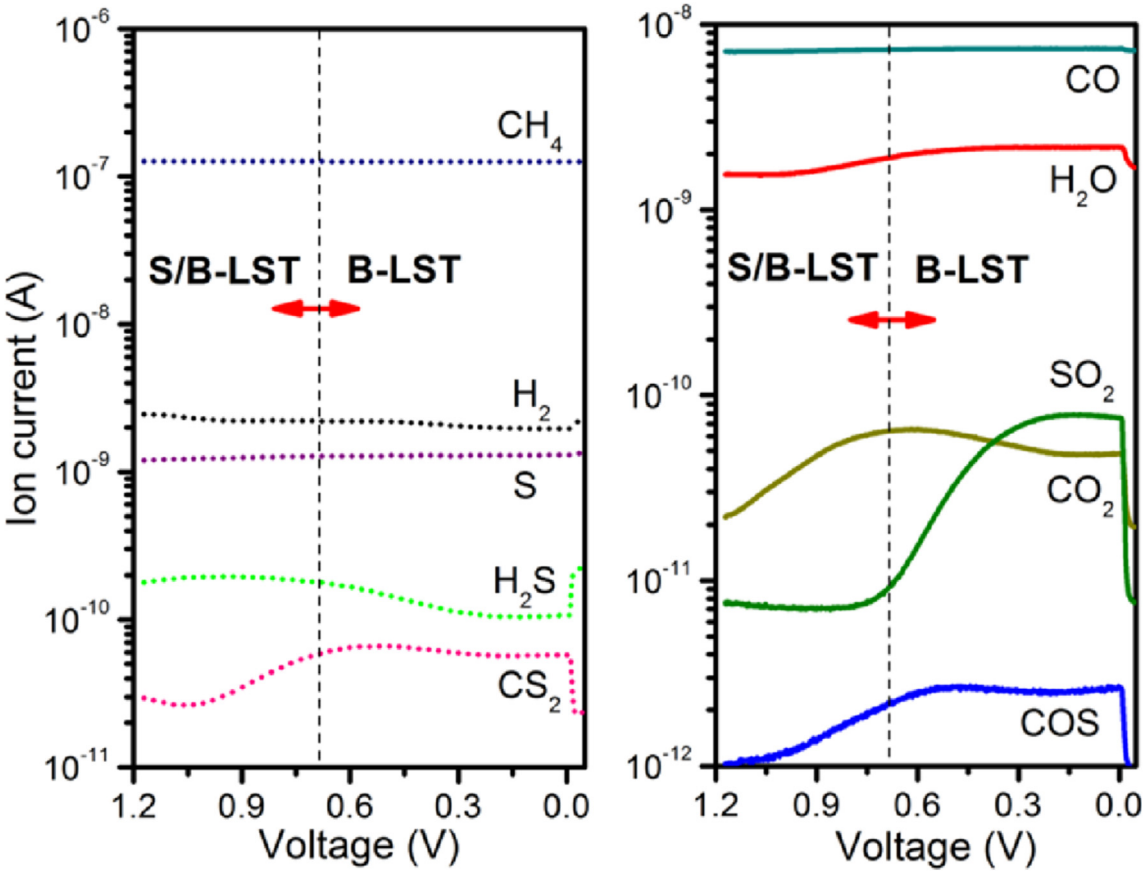

Fig. 5. Mass spectrometric signals of anode effluent as a function of cell voltage, SOFC was operated potentio-dynamically with a scan rate of 0.2 mV s^{-1} at 800° in 0.5% H_2S/CH_4 with S/B-LST anode.

methane (443.67 Ω cm^2), reflecting its poor activity towards methane oxidation. In comparison, R_p value was only 21.53 Ω cm^2 for S/B-LST anode. This dramatic difference strongly supported the catalytic promoting effects of surface sulfur species. Though less active than conventional transition metal catalysts, they significantly outperformed several perovskite oxide anodes regarding methane oxidation [44].

Intuitively, one would imagine that the possible oxidation of H_2S may contribute to the enhanced electrochemical performances. In our previous work, we showed such low concentration of H_2S was unable to power a SOFC by itself [26]. In this work, we monitored the concentration variation of H_2S as a function of overpotential in Fig. 5. Interestingly, consumption of H_2S only occurred when cell was deeply biased [12]. Thus, when the voltage was higher than ~ 0.7 V, the surface sulfur was sustained on S/B-LST. Otherwise, H_2S and SO_2 signals would vary. The generated electrical current in SOFC mainly came from the conversion of methane as CO_2 and H_2O signals intensified. The presence of COS and CS_2 was attributable to the reaction intermediates of the sulfur promoted methane activation (see below).

Conversely, when the voltage was below 0.7 V, the consumption of H_2S as well as the production of SO_2 was initiated. Simultaneously, the oxidation of methane was substantially decelerated and the signals of H_2O, CO_2, CS_2 and COS were stabilized or even decreased. Because the current was still increasing in step with the degree of polarization (see Fig. 4a), H_2S became the only contributing fuel. Under this condition (high pO_2), the surface sulfur species, particularly those in the vicinity of TPB, must be oxidized according to the thermodynamic prediction [47,48]. We therefore maintained that the actual anode became B-LST. This transformation completed at ~0.3 V and was accompanied by the drastically drop of cell performances (see Figs. 4a and 5): in the I-V curve, a huge overpotenital was recorded in the same voltage region (0.3~0 V), and the electric current started to decrease even when the bias was still increasing! This scenario contradicted the commonly observed abrupt current increase when cell was deeply biased, in which the oxygen spillover mechanism caused expansions of the actual triple-phase boundary (see Fig. S6 for details) [49]. Thus, we asserted that the surface sulfur species are indeed the promoters of methane electrochemical conversion. Evidences were also seen during fuel switching where adsorption-desorption of sulfur species was associated (see Fig. S7).

3.4. Hypothetic pathway of S-promoted methane conversion

The sulfur species bond with Ti metal center, creating active sites for methane activation [50,51]. This weak interaction (sulfur adsorption on titanate was reversible, but on Ni, the chemisorption was not fully reversible [52]) actually facilitates the C—H bonds activation of methane as revealed by recent studies [25]. The physisorbed elemental sulfur, which was more weakly bound on S/B-LST, can be even more active according to this theory. The activation procedure was presumably similar to that proposed by Froment and Marks [25,53], the adsorbed sulfur species was denoted as $S_{(ad)}$ in the following equations:

Activation:

$$CH_4 + S_{(ad)} \rightarrow CH_4 \cdots S_{(ad)} \quad (6)$$

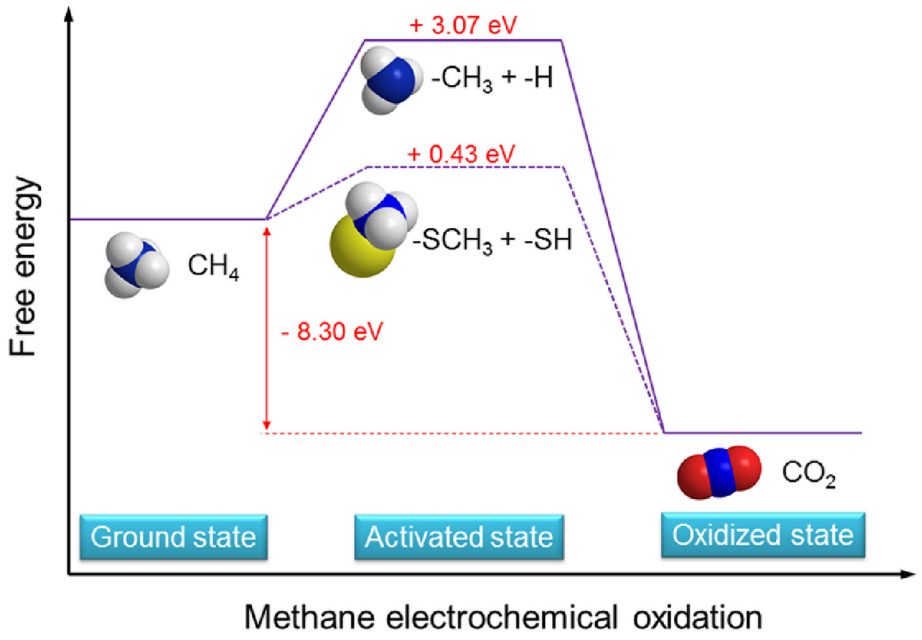

Fig. 6. A comparison of the energy barriers for direct and sulfur-promoted methane activation.

$$CH_4\cdots S_{(ad)} + S_{(ad)} \rightarrow CH_3{-}S_{(ad)} + H{-}S_{(ad)} \quad (7)$$

$$CH_3{-}S_{(ad)} + S_{(ad)} \rightarrow CH_2{-}S_{(ad)} + H{-}S_{(ad)} \quad (8)$$

$$CH_2{-}S_{(ad)} + S_{(ad)} \rightarrow CH{-}S_{(ad)} + H{-}S_{(ad)} \quad (9)$$

$$CH{-}S_{(ad)} + S_{(ad)} \rightarrow C{-}S_{(ad)} + H{-}S_{(ad)} \quad (10)$$

$$C{-}S_{(ad)} + S_{(ad)} \rightarrow CS_2\uparrow \quad (11)$$

CS_2 would be evolved from methane activation process. The origins of COS, H_2O and CO_2 might be complicated, a possible route using a Langmuir-Hinshelwood model can be:

Oxidation:

$$S_{(ad)} + O^{2-} \rightarrow O{-}S_{(ad)} + 2e^- \quad (12)$$

$$H{-}S_{(ad)} + O{-}S_{(ad)} \rightarrow HO{-}S_{(ad)} \quad (13)$$

$$HO{-}S_{(ad)} + H{-}S_{(ad)} \rightarrow H_2O\uparrow + 2S_{(ad)} \quad (14)$$

$$C{-}S_{(ad)} + O{-}S_{(ad)} \rightarrow OC\text{-}S_{(ad)} + S_{(ad)} \quad (15)$$

$$OC\text{-}S_{(ad)} \rightarrow COS\uparrow \quad (16)$$

$$OC{-}S_{(ad)} + O{-}S_{(ad)} \rightarrow CO_2\uparrow + 2S_{(ad)} \quad (17)$$

Note that carbon oxidation reaction was usually the rate-determined step in methane oxidation [53]. This promoting effect became invalid when the $S_{(ad)}$ species were oxidized if the cell voltage dropped to below ~0.7 V producing SO_2.

Over-oxidation:

$$O{-}S_{(ad)} + O^{2-} \rightarrow SO_2\uparrow + 2e^- \quad (18)$$

The promoted activation of methane by sulfur was also supported by the thermodynamic calculation data shown in Fig. 6. In comparison with the thermal activation of methane yielding $-CH_3$ and $-H$, the sulfur-assisted process decreased the energy barrier significantly from 3.07 eV to 0.43 eV at 800 °C, assuming the formation of $-SCH_3$ and $-SH$ species.

4. Conclusions

In this study, we understood that LST anode underwent significant surface changes during SOFC operation in H_2S-containing methane. A surface shell of amorphous disordered layer was observed, causing discolorations of the catalyst. The surface sulfur layer was ~1 nm thick, consisting of $-S$, $-SH$ and elemental sulfur species. The combination of the disordered LST shell and sulfur layer promoted the electrochemical oxidation of methane in SOFC.

Acknowledgements

This research was supported through a Strategic Project Grant, funding to the Solid Oxide Fuel Cell Canada Strategic Research Network from the Natural Science and Engineering Research Council (NSERC) and the RIEM project from NSERC-MRS and CanmetMATERIALS. We thank A. Seyeux from Institut de Recherche de Chimie Paris (Physical Chemistry of Surfaces Group), Chimie ParisTech, for performing the ToF-SIMS analyses, the French Embassy for financial support, and the Région Ile-de-France for financial support for the XPS and ToF-SIMS equipment. This work is part of the Research Priority Area Sustainable Chemistry of the University of Amsterdam, http://suschem.uva.nl.

Appendix A. Supplementary data

Supplementary data related to this article can be found at http://dx.doi.org/10.1016/j.jpowsour.2017.01.048.

References

[1] C. Li, Y. Shi, N. Cai, J. Power Sources 195 (2010) 4660–4666.
[2] J. Mirzababaei, L.-S. Fan, S.S.C. Chuang, J. Mater. Chem. A 3 (2015) 2242–2250.
[3] B. Hua, N. Yan, M. Li, Y.-q. Zhang, Y.-f. Sun, J. Li, T. Etsell, P. Sarkar, K. Chuang, J.-L. Luo, Energy Environ. Sci. 9 (2016) 207–215.
[4] S.P. Jiang, S.H. Chan, J. Mater. Sci. 39 (2004) 4405–4439.
[5] Y. Chen, Y. Zhang, Y. Lin, Z. Yang, D. Su, M. Han, F. Chen, Nano Energy 10

(2014) 1–9.
[6] L. Yang, S. Wang, K. Blinn, M. Liu, Z. Liu, Z. Cheng, M. Liu, Science 326 (2009) 126–129.
[7] X. Zhou, N. Yan, K.T. Chuang, J. Luo, RSC Adv. 4 (2014) 118–131.
[8] V.C.H. Kroll, H.M. Swaan, C. Mirodatos, J. Catal. 161 (1996) 409–422.
[9] F. Besenbacher, I. Chorkendorff, B.S. Clausen, B. Hammer, A.M. Molenbroek, J.K. Norskov, I. Stensgaard, Science 279 (1998) 1913–1915.
[10] T.V. Choudhary, V.R. Choudhary, Angew. Chem. Int. Ed. 47 (2008) 1828–1847.
[11] X. Li, M. Liu, J.-p. Lee, D. Ding, L.A. Bottomley, S. Park, M. Liu, Phys. Chem. Chem. Phys. 17 (2015) 21112–21119.
[12] Z. Cheng, J.-H. Wang, Y. Choi, L. Yang, M.C. Lin, M. Liu, Energy Environ. Sci. 4 (2011) 4380–4409.
[13] N. Yan, J. Pandey, Y.M. Zeng, B.S. Amirkhiz, B. Hua, N.J. Geels, J.L. Luo, G. Rothenberg, ACS Catal. 6 (2016) 4630–4634.
[14] A. Garcia, N. Yan, A. Vincent, A. Singh, J.M. Hill, K.T. Chuang, J.L. Luo, J. Mater. Chem. A 3 (2015) 23973–23980.
[15] M.Q. Liu, S.L. Wang, T. Chen, C. Yuan, Y.C. Zhou, S.R. Wang, J. Huang, J. Power Sources 274 (2015) 730–735.
[16] L. Adijanto, V.B. Padmanabhan, R. Kuengas, R.J. Gorte, J.M. Vohs, J. Mater. Chem. 22 (2012) 11396–11402.
[17] S.W. Tao, J.T.S. Irvine, Nat. Mater. 2 (2003) 320–323.
[18] Y.H. Huang, R.I. Dass, Z.L. Xing, J.B. Goodenough, Science 312 (2006) 254–257.
[19] S. Sengodan, S. Choi, A. Jun, T.H. Shin, Y.-W. Ju, H.Y. Jeong, J. Shin, J.T.S. Irvine, G. Kim, Nat. Mater. 14 (2015) 205–209.
[20] D. Neagu, T.-S. Oh, D.N. Miller, H. Menard, S.M. Bukhari, S.R. Gamble, R.J. Gorte, J.M. Vohs, J.T.S. Irvine, Nat. Commun. 6 (2015), 8120–8120.
[21] B. Hua, N. Yan, M. Li, Y.-F. Sun, Y.-Q. Zhang, J. Li, T. Etsell, P. Sarkar, J.-L. Luo, Adv. Mater. 28 (2016) 8922–8926.
[22] D. Neagu, G. Tsekouras, D.N. Miller, H. Menard, J.T.S. Irvine, Nat. Chem. 5 (2013) 916–923.
[23] M.R. Afshar, N. Yan, B. Zahiri, D. Mitlin, K.T. Chuang, J.-L. Luo, J. Power Sources 274 (2015) 211–218.
[24] L. Deleebeeck, M. Shishkin, P. Addo, S. Paulson, H. Molero, T. Ziegler, V. Birss, Phys. Chem. Chem. Phys. 16 (2014) 9383–9393.
[25] Q. Zhu, S.L. Wegener, C. Xie, O. Uche, M. Neurock, T.J. Marks, Nat. Chem. 5 (2013) 104–109.
[26] M. Roushanafshar, N. Yan, K.T. Chuang, J.-L. Luo, Appl. Catal. B 176–177 (2015) 627–636.
[27] H.M.T. Galvis, J.H. Bitter, C.B. Khare, M. Ruitenbeek, A.I. Dugulan, K.P. de Jong, Science 335 (2012) 835–838.
[28] Z. Cheng, M.L. Liu, Solid State Ionics 178 (2007) 925–935.
[29] M.B. Pomfret, J.C. Owrutsky, R.A. Walker, J. Phys. Chem. B 110 (2006) 17305–17308.
[30] H.H.M. Thi, B. Saubat, N. Sergent, T. Pagnier, Solid State Ionics 272 (2015) 84–90.
[31] G. Nurk, T. Huthwelker, A. Braun, C. Ludwig, E. Lust, R. Struis, J. Power Sources 240 (2013) 448–457.
[32] C. Lee, J. Yahia, J.L. Brebner, Phys. Rev. B 3 (1971) 2525–2533.
[33] M. Higuchi, K. Aizawa, K. Yamaya, K. Kodaira, J. Solid State Chem. 92 (1991) 573–577.
[34] H. Tan, Z. Zhao, W.-b. Zhu, E.N. Coker, B. Li, M. Zheng, W. Yu, H. Fan, Z. Sun, ACS Appl. Mater. Interfaces 6 (2014) 19184–19190.
[35] J.C. Ruiz-Morales, J. Canales-Vazquez, C. Savaniu, D. Marrero-Lopez, W.Z. Zhou, J.T.S. Irvine, Nature 439 (2006) 568–571.
[36] D. Chu, A. Younis, S. Li, J. Phys. D. Appl. Phys. 45 (2012).
[37] X. Chen, L. Liu, P.Y. Yu, S.S. Mao, Science 331 (2011) 746–750.
[38] T. Lu, O.Y. Ti, K.P. Loh, J.J. Vittal, J. Mater. Chem. 16 (2006) 272–277.
[39] W.D. Schneider, B. Delley, E. Wuilloud, J.M. Imer, Y. Baer, Phys. Rev. B 32 (1985) 6819–6831.
[40] J.N. Kuhn, N. Lakshminarayanan, U.S. Ozkan, J. Mol. Catal. A Chem. 282 (2008) 9–21.
[41] T.A. Carlson, G.E. McGuire, J. Electron. Spectrosc. Relat. Phenom. 1 (1972) 161–168.
[42] B.R. Strohmeier, Surf. Interface Anal. 15 (1990) 51–56.
[43] P. Marcus, C. Hinnen, D. Imbert, J.M. Siffre, Surf. Interface Anal. 19 (1992) 127–132.
[44] S. Lee, G. Kim, J.M. Vohs, R.J. Gorte, J. Electrochem. Soc. 155 (2008) B1179–B1183.
[45] A.L. Vincent, J.-L. Luo, K.T. Chuang, A.R. Sanger, Appl. Catal. B 106 (2011) 114–122.
[46] R. Barfod, A. Hagen, S. Ramousse, P.V. Hendriksen, M. Mogensen, Fuel Cells 6 (2006) 141–145.
[47] A.K. Dalai, E.L. Tollefson, Can. J. Chem. Eng. 76 (1998) 902–914.
[48] T. Mattisson, M. Johansson, A. Lyngfelt, Fuel 85 (2006) 736–747.
[49] S.H. Chan, K.A. Khor, Z.T. Xia, J. Power Sources 93 (2001) 130–140.
[50] J.A. Rodriguez, S. Chaturvedi, M. Kuhn, J. Hrbek, J. Phys. Chem. B 102 (1998) 5511–5519.
[51] E. Shustorovich, R.C. Baetzold, Science 227 (1985) 876–881.
[52] J. Hepola, P. Simell, Appl. Catal. B 14 (1997) 305–321.
[53] J.G. Xu, G.F. Froment, AlChE J. 35 (1989) 88–96.